Journal of Catalysis 408 (2022) 1–8

Contents lists available at ScienceDirect

Journal of Catalysis

journal homepage: www.elsevier.com/locate/jcat

Visualisation and quantification of flooding phenomena in gas diffusion electrodes used for electrochemical CO_2 reduction: A combined EDX/ICP–MS approach

Ying Kong [a,b], Huifang Hu [a], Menglong Liu [a,b], Yuhui Hou [a,b], Viliam Kolivoška [c], Soma Vesztergom [a,d,*], Peter Broekmann [a,b,*]

[a] University of Bern, Department of Chemistry, Biochemistry and Pharmaceutical Sciences, Freiestrasse 3, 3012 Bern, Switzerland
[b] National Centre of Competence in Research (NCCR) Catalysis, University of Bern, Freiestrasse 3, 3012 Bern, Switzerland
[c] J. Heyrovský Institute of Physical Chemistry of the Czech Academy of Sciences, Dolejškova 2155/3, 18223 Prague, Czech Republic
[d] Eötvös Loránd University, Department of Physical Chemistry, Pázmány Péter sétány 1/A, 1117 Budapest, Hungary

ARTICLE INFO

Article history:
Received 7 January 2022
Revised 10 February 2022
Accepted 15 February 2022
Available online 22 February 2022

Keywords:
Carbon dioxide electroreduction
Gas diffusion electrodes
Flooding
Precipitate formation

ABSTRACT

The most promising strategy to scale up the electrochemical CO_2 reduction reaction (*ec*-CO_2RR) is based on the use of gas diffusion electrodes (GDEs) that allow current densities close to the range of 1 A/cm^2 to be reached. At such high current densities, however, the flooding of the GDE cathode is often observed in CO_2 electrolysers. Flooding hinders the access of CO_2 to the catalyst, and by thus leaving space for (unwanted) hydrogen evolution, it usually leads to a decrease of the observable Faradaic efficiency of CO_2 reduction products. To avoid flooding as much as possible has thus become one of the most important aims of to-date *ec*-CO_2RR engineering, and robust analytical methods that can quantitatively assess flooding are now in demand. As flooding is very closely related to the formation of carbonate salts within the GDE structure, in this paper we use alkali (in particular, potassium) carbonates as a tracer of flooding. We present a novel analytical approach —based on the combination of cross-sectional energy-dispersive X-ray (EDX) mapping and inductively coupled plasma mass spectrometry (ICP–MS) analysis— that can not only visualise, but can also quantitatively describe the electrolysis time dependent flooding in GDEs, leading to a better understanding of electrolyser malfunctions.

1. Introduction

Great progress has recently been made towards the development of new technologies that enable a large-scale reduction of the atmospheric concentration of CO_2, one of the most important contributors of global warming [1]. Among these technologies, electrochemical ones deserve special attention as electrolysers — ideally powered by renewable energy sources— can effectively be used to convert CO_2 into a variety of commodity chemicals and synthetic fuels, such as CO, formic acid, different alcohols and hydrocarbons [2].

In the past few years, the efficiency of newly developed catalysts for the electrochemical CO_2 reduction reaction (*ec*-CO_2RR) has become so high that under ambient conditions it is not any longer the catalytic activity but rather the limited rate of liquid-phase CO_2 transport that hinders the process [3]. Several attempts have thus been made to boost *ec*-CO_2RR by increasing the rate of CO_2 transport, and the most promising of these scale-up strategies involve the use of gas diffusion electrodes (GDEs) [4–7].

The use of GDEs enables current densities that are at least one order of magnitude larger than those measurable in standard H-type cells [3,7]. The benefit of achieving high currents comes, however, at the cost of stability issues, and it is primarily the rapid flooding of GDEs that raises most concerns [7–11].

CO_2 electrolysers where the catalyst dispersed over a gas diffusion layer (GDL) contacts the electrolyte solution through a wet membrane —that is, in so-called zero-gap cathode half-cell configurarions [7]— flooding usually occurs at high current densities where either the CO_2 reduction reaction itself or its parasitic side-process, hydrogen evolution reaction (HER) cause a significant

* Corresponding authors at: University of Bern, Department of Chemistry, Biochemistry and Pharmaceutical Sciences, Freiestrasse 3, 3012 Bern, Switzerland (P. Broekmann); Eötvös Loránd University, Department of Physical Chemisty, Pázmány Péter sétány 1/A, 1117 Budapest, Hungary (S. Vesztergom).

E-mail addresses: ying.kong@unibe.ch (Y. Kong), huifang.hu@unibe.ch (H. Hu), menglong.liu@unibe.ch (M. Liu), viliam.kolivoska@jh-inst.cas.cz (V. Kolivoška), vesztergom@chem.elte.hu (S. Vesztergom), peter.broekmann@dcb.unibe.ch (P. Broekmann).

https://doi.org/10.1016/j.jcat.2022.02.014
0021-9517/

near-electrode *p*H increase. The CO_2 supply of the GDE reacts with the electro-generated OH^- ions, which leads to the localised formation of carbonate salts that in turn increases the wettability [8–10] of the GDE and intensifies flooding.

As flooding limits the access of CO_2 to the catalyst, it usually leads to a decrease of the observable Faradaic efficiency of CO_2 reduction products, and leaves space for unwanted hydrogen evolution. To suppress flooding as much as possible, and to understand its mechanism and key factors has thus become one of the most important aims of to-date *ec*-CO_2RR research, and analytical tools that can quantitatively assess the means and extent of flooding are now in demand.

The mechanism of flooding depends on several processes occurring in GDE-based CO_2 electrolysers, and system properties influencing flooding include the wettability of GDEs [12–17] and its dependence on the applied electrode potential (also called electrowetting [18]), the flow-rate [19] and humidity [20,21] of the CO_2 supply, the presence of reaction products [10], and the thickness of the employed membrane [17]. Flooding is very often accompanied by the massive formation of carbonate precipitates on-top, and within deeper layers of the GDE [7–11,18,22–24], and the amount and distribution of carbonates —in case of CO_2 electrolysers operated with a KOH anolyte, these are typically potassium carbonates and bicarbonates— seem to be an important tracer of flooding within the three-dimensional GDE structure.

The aim of this paper is to show that the post-electrolysis analysis of GDE samples by energy-dispersive X-ray (EDX) elemental mapping can easily be used to visualise the electrolysis time dependent penetration of K^+-containing precipitates into the GDE. In order to make the obtained distribution profiles comparable for electrodes that received different electrolysis treatments, it is necessary to convert the relative distribution profiles to absolute concentration *vs.* depth plots that already bear quantitative information. This latter aim can be achieved by an inductively coupled plasma mass spectrometry (ICP–MS)-based determination of the total potassium content of the GDE [25]. The described EDX/ICP–MS combination is a powerful and very robust technique that allows a better understanding of *ec*-CO_2RR electrolyser malfunctions by enabling the accurate visualisation and quantification of flooding phenomena in GDE samples.

2. The method

The scheme of a typical gas-fed CO_2 electrolyser employing a zero-gap cathode half-cell configuration is shown in Fig. 1, with the blown-up section depicting the GDE cathode in direct contact with the anion exchange membrane. The GDE cathode is created by evenly covering the surface of a gas diffusion layer (GDL) with a catalyst ink that can be achieved by using several techniques [3] including drop-casting, airbrushing, vacuum filtering, etc. The uniformity of the catalyst layer thickness depends however not only on the applied technique but also on the imperfections of the gas diffusion layer: especially cracks found on the GDL surface (see, *e.g.*, Fig. 5.b in Section 4) may lead to non-uniform coverage [26–28] and to the burial of some catalyst particles in deeper trenches.

The GDL itself is a bilayer structure that consists of an upper (microporous) and an underlying (fibrous) layer. The microporous layer acts as an electrically conductive mechanical support to the catalyst, holding it in direct contact with the membrane. In many electrolysers, the applied catalyst ink contains silver nanoparticles that direct *ec*-CO_2RR towards the formation of CO as a dominant reaction product [8,11,17,21,24,29]. Note here that CO belongs to the most economically viable *ec*-CO_2RR products [30] and has large global annual production [3]. The cathode reaction of CO_2-to-CO conversion can be written as

$$CO_2 + H_2O + 2e^- \rightarrow CO + 2OH^-, \quad (1)$$

and the operation of the electrolyser should be optimised so that parasitic hydrogen evolution reaction (HER),

$$2H_2O + 2e^- \rightarrow H_2 + 2OH^-, \quad (2)$$

would take place only incidentally.

In the design shown in Fig. 1, a constant (humidified) CO_2 flow penetrates the fibrous part of the GDL, and the CO_2 molecules are transported through the pores of the thin microporous layer to reach the catalyst where they are reduced to CO.

The (essentially wet) membrane has two important roles in the electrolyser: one is that it enables water (a reactant of *ec*-CO_2RR) to access the catalyst, and another is that it allows the passage of the formed OH^- ions (a by-product of CO_2 reduction) from the cathode surface to the anode compartment of the cell. The anode compartment is filled with a solution of KOH, and OH^- ions are oxidised on the Ir anode to form O_2 gas:

$$4OH^- \rightarrow 2H_2O + O_2 + 4e^-. \quad (3)$$

The wettability of the GDL plays a crucial role in determining the cathode performance of gas-fed CO_2 electrolysers. The presence of some amount of water, based on Eq. (1), is essential; however, if too much water enters the GDL structure, it may block the access of CO_2 to the catalyst, shifting the balance of the cathode reaction from the preferred *ec*-CO_2RR towards the parasitic HER [31].

For this reason, GDLs are usually made hydrophobic by the manufacturer (*e.g.*, by a treatment with polytetrafluoroethylene, PTFE) and the conditions of the electrolysis are optimized to uphold hydrophobicity as long as possible. From this point of view, the imperfections of the anion exchange membrane deserve special attention, especially if the membrane allows not only the transfer of OH^- ions, but also the transference of cations. As the real-life behaviour of anion exchange membranes is far from ideal [32], the transference of cations very often occurs, and for example in case of the electrolyser shown by Fig. 1, K^+ ions of the anolyte can thus appear on the cathode side of the cell.

The alkalination of the cathode surface —note that OH^- ions are produced both by Reaction (1) and (2)— clearly acts as a driving force for the transport of K^+ ions from the anode compartment to the cathode, where the alkaline conditions and the presence of CO_2 facilitate the formation of K_2CO_3 or $KHCO_3$ salts. If concentrations are high enough [9], both K_2CO_3 and $KHCO_3$ can form precipitates on-top and within the deeper layers of the GDE. This reduces the hydrophobicity of the GDE and triggers flooding, which ultimately breaks down the overall cell performance.

There seems to be a consensus in literature with regard to that the formation of carbonate precipitates on the cathode side of *ec*-CO_2RR electrolysers is an important indicator of flooding [9–11,20,21,33,34]. In spite of this, scanning electron microscopy (SEM)-based imaging techniques like EDX elemental mapping have only scarcely been used to study the penetration of carbonate precipitates into GDE structures [7,11,34]. The reason behind this is obvious: while EDX elemental (K) mapping, applied in a cross-sectional view to study the penetration of K_2CO_3/$KHCO_3$ precipitates into the GDE structure can give a good qualitative picture about the relative distribution of the formed K^+ salts, the comparison of such elemental maps is by no means straightforward. Such comparisons would require EDX elemental mapping to provide truly quantitative information, which is usually not the case.

Indeed, the quantification of elemental maps is a very demanding task that would not only necessitate the acquisition, storage, and subsequent analysis of entire spectra, pixel-by-pixel [35], but it would also require the in-depth understanding of electron

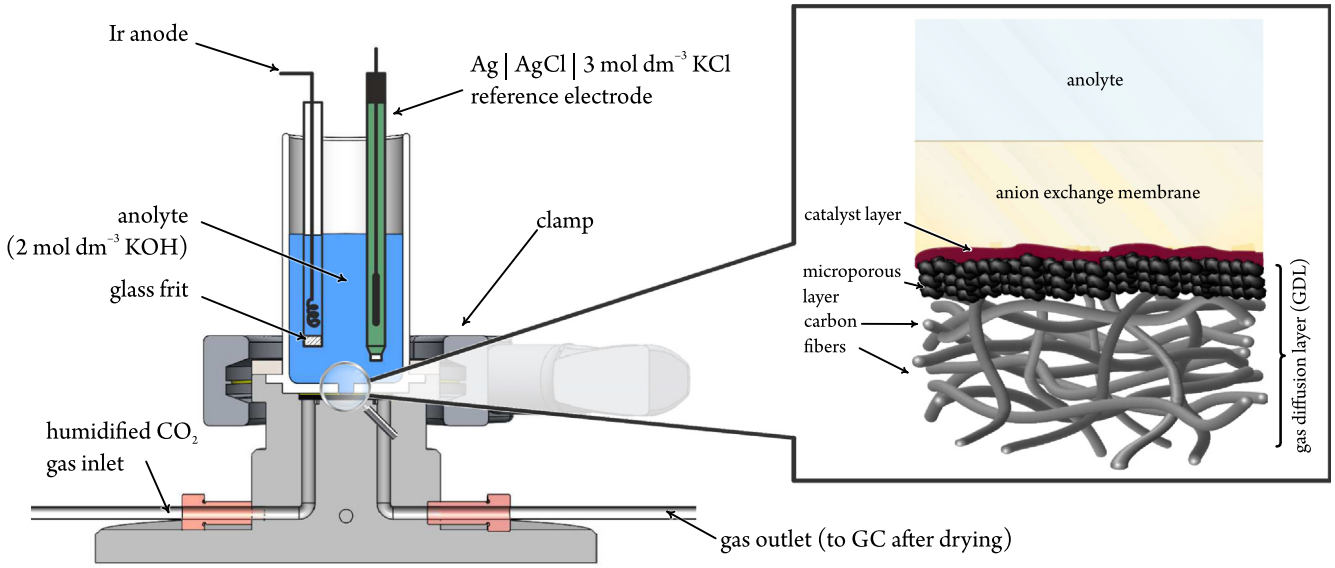

Fig. 1. Scheme of a gas-flow CO_2 electrolyser employing a zero-gap cathode half-cell configuration. The gas diffusion electrode/membrane assembly is shown by the inset at the initial stage of electrolysis.

beam/material interactions, which is particularly challenging when working with heterogeneous and highly porous materials (*e.g.*, GDEs).

X-ray signal intensities are known to depend largely on (amongst other parameters) the applied acceleration voltage [35], and this is exemplarily demonstrated by the cross-sectional EDX elemental (K) maps of Fig. 2. These maps, taken at different applied accelerating voltages, show the same GDE sample that exhibits marks of *ec*-CO_2RR-induced K_2CO_3/$KHCO_3$ precipitation within its structure.

Maps of the top row of Fig. 2 are those shown by the operating software of the SEM instrument. The automatic colouration of these maps is optimised for human perception, and as a result, the maps could lead us to the erroneous conclusion that the potassium concentrations visualised by them are markedly different. As, however, the four maps are made of the very same sample, this is certainly not the case: the maps are differently coloured only because the corresponding K peaks in the EDX spectra become more intense at higher accelerating voltages.

Fortunately, from most SEM operating software, EDX maps can be exported not only in the form of images but also in the form of two-dimensional numerical arrays that represent the (in our case, K) signal intensities over the sampled area. If we create such numerical representations from the four maps shown in the top row of Fig. 2, we get four arrays on which we can perform mathematical operations. We can, for example, normalise the arrays to their (overall) maximum, and we can then convert the arrays back into images. If we use the same colour-code that was applied before, we obtain the images shown by the middle row of Fig. 2. These coloured maps already give a trustworthy representation of intensity ratios; however, at low accelerating voltages, the normalised intensities happen to be so low that we see almost entirely dark fields.

In order to reduce the dependency of intensities on the applied accelerating voltage, we have to normalise each array individually, using their respective maxima as an individual norm. By this approach, we get to the images shown in the bottom row of Fig. 2. These elemental maps, while they all appear a bit dark for the human eye, all look essentially the same. Subtle differences between the images do exist, however, primarily because not only the overall intensity of the spectrum peaks but also the penetration depth of the electron beam depends on the accelerating voltage [35]. This dependence, while it affects the measured absolute intensities, exerts only a minor effect on the observed relative intensity distributions.

The above two normalisation concepts are illustrated also by the graphs of Fig. 2 that contain sums of intensities for each image row, plotted *vs.* the respective row index. The graphs clearly show that while the recorded K signal intensity does vary greatly with the applied accelerating voltage, and while the exact relationship between local K concentration and intensity may not be known, EDX mapping is still robust enough to deliver a relative distribution of potassium-containing precipitates along the line normal to the GDE surface.

Such relative distributions, obtained from GDEs that had undergone different *ec*-CO_2RR stressing treatment can of course not directly be compared, unless we determine by some other analytical method the total potassium content of the GDE. A variety of elemental analysis methods can be used to achieve this goal; in our practice we favour ICP–MS-based determination.

The essence of the method described here is schematically shown in Fig. 3. On the top surface of GDEs that have previously been used for *ec*-CO_2RR, the appearance of precipitates is usually visible already to the bare eye. The centrally located, salt-covered part (of known geometric area) is removed by a punching blade, and the resulting 'coin' is cut into two by a sharp knife. One part of the coin is briefly sonicated and then left for over-night in a known volume (usually 1 cm^3) of cc. HNO_3, so that its K_2CO_3/$KHCO_3$ content is quantitatively leached. The concentration of the resulting solution is then determined by ICP–MS in known (usually 500 or 1000 times) dilutions: by this method, the total potassium mass that is contained by the given volume of the GDE is calculated and normalised to the base area of the analysed sample. This yields a total surface area-normalised concentration that is usually in the range of a few mg cm^{-2}.

The other half of the coin (Fig. 3) is used for cross-sectional EDX K elemental mapping, without any additional treatment other than drying the sample. In order to improve statistics, usually multiple locations of the same cut are mapped, and sometimes, even additional cuts are made and sampled. The resulting EDX maps are then exported in numerical form, and depth profiles of the relative K distribution are created by row-wise summation. Row indices

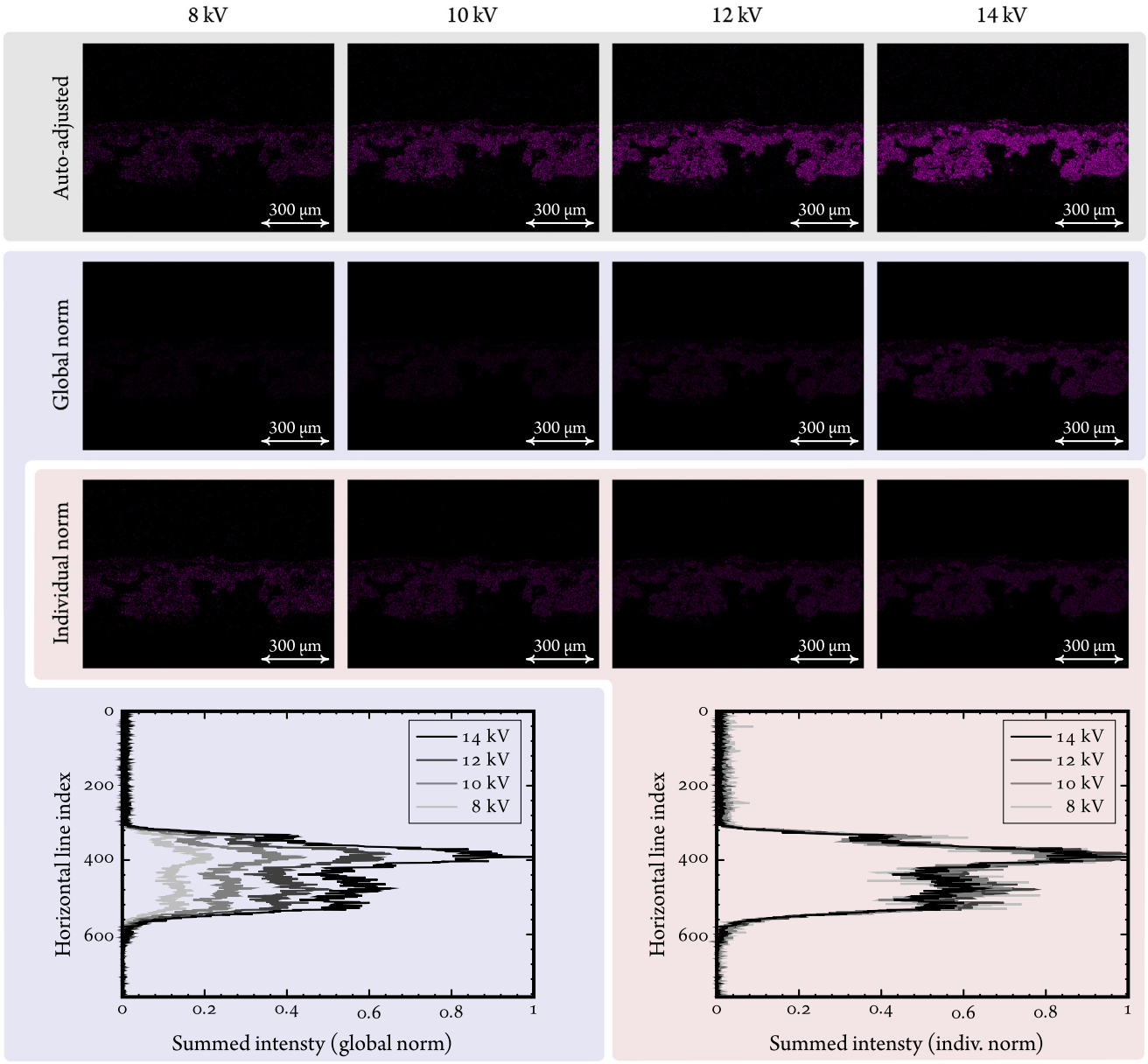

Fig. 2. Electrolysis-induced potassium penetration into a GDE sample visualised by EDX elemental maps (cross-sectional view), recorded using different accelerating voltages as shown. Images of the same column show maps of the exact same intensity dataset, coloured differently. The brightness and the contrast of images in the top row was automatically adjusted for optimal perception by the human eye — this is how most SEM operating software would show these maps. Colour intensities in the middle row were normalised to the largest intensity value detected. In case of the third row, the maps were normalised individually, each to its own maximum intensity. The graphs show the differences of the two normalisation concepts in row-by-row intensity summation. The EDX measurements were made on sample GDE#2, following passage of −1839 C cm^{-2} charge (cf. to Sections 3 and 4, as well as to Fig. 5).

are turned into spatial coordinates knowing the resolution of the map.

The individual relative distributions are aligned on the distance scale by means of (differential) edge detection, and an averaged curve is calculated. The relative distributions are subsequently re-scaled into absolute concentration profiles (usually expressed in units of µg cm^{-3}); the applied scaling factor is chosen so that the full space integral of the averaged absolute concentration profile equals the surface area-normalised concentration determined by ICP–MS.

The described cross-sectional EDX/ICP–MS combination approach yields concentration depth profiles that are comparable for GDE samples that are either of different original structure or that underwent different *ec*-CO_2RR stressing treatment (see later Fig. 5), and can lead to a better understanding of flooding-related phenomena. Note here that in order to obtain statistically reliable data, both the ICP–MS and the EDX mapping measurements are to be repeated several times, using GDE samples that received the very same treatment. As it will be shown later in Fig. 5, this approach helps to identify possible outliers. Also note that ICP–MS measurements may not have to be performed on all (rather just on a few) studied samples, which may reduce the time demand of the analysis.

As the described EDX/ICP–MS combination approach is a post-experimental characterisation technique, it cannot be used for a real-time observation of flooding-related phenomena like it is possible, for example, in *operando* tomographic X-ray absorption spectroscopy [36]. The EDX/ICP–MS combination is, however, a more

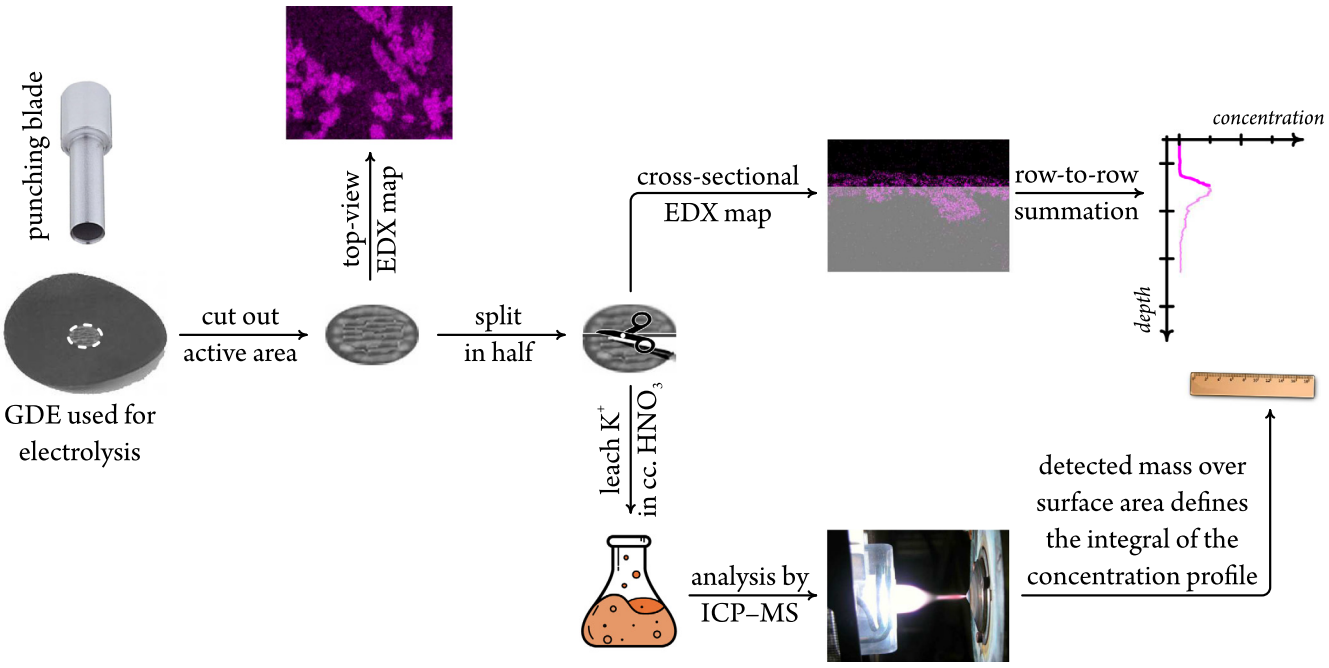

Fig. 3. The strategy to quantitatively assess flooding phenomena in GDEs uses $K_2CO_3/KHCO_3$ precipitates as a tracer of flooding. Following electrolysis, the carbonate precipitates formed over the GDE are visible to the bare eye (and can also be seen by top-down EDX mapping). By cross-sectional EDX, the relative distribution of K can be mapped along the surface normal. Absolute concentration (mass over volume) profiles can be created by applying a scaling factor that sets the integral of the profile equal to the (surface area normalised) K mass determined by ICP–MS analysis.

robust and a considerably cheaper method than X-ray absorption or scattering measurements that require specially designed cells and a significant amount of synchrotron beam-time, and the amount of information gathered from EDX/ICP–MS studies may effectively complement the results of *operando* investigations.

The versatility of the method will be illustrated in Section 4, where we used two different gas diffusion electrodes for CO_2 electrolysis in a gas-fed CO_2 electrolyser employing a zero-gap cathode half-cell configuration, finding that the different structure of the two GDLs result in different $K_2CO_3/KHCO_3$ deposition patterns and, ultimately, different electrolyser stabilities.

3. Experimental

Two commercial gas diffusion layers (Table 1), a Freudenberg H23C8 (GDL#1) and a Sigracet 36BB (GDL#2) paper, were used in this study. The microporous layers of both GDLs contain ~ 5% PTFE as a water repelling agent.

To prepare a catalyst ink, 4.5 mg of silver nanowires (Ag NWs, prepared as described in [37]) and 0.8 mg of carbon black (VULCAN^{TM} VXC72R, Cabot) were separately dispersed in 20 cm^3 of isopropanol (BASF SE, assay ⩾ 99.0%) by half hour of sonication. Both suspensions were intermixed and sonicated for an additional half hour, then dried by a rotary evaporator (Büchi R210, 40 °C, 65 mbar). The resulting mixture was then re-dispersed in 18 cm^3 of isopropanol containing 180 $\mu\ell$ of Nafion 117 solution (Sigma–Aldrich, ~ 5 wt% in a mixture of lower aliphatic alcohols and water) and subjected to 20 min of sonication. Subsequently, the resulting ink was carefully dispersed by using an airbrush pistole (Infinity CR plus) propelled by nitrogen gas (99.999%, Carbagas, Switzerland) onto the GDL substrate.

Table 1
Parameters of the gas diffusion layers used in this study.

	GDL#1, Freudenberg H23C8	GDL#2, Sigracet 36BB
Microporous layer thickness*	41 µm	97 µm
Fibrous layer thickness*	194 µm	160 µm
Electrical resistivity†	8 mΩ cm^2	9 mΩ cm^2
Area density†	135 g cm^{-2}	105 g cm^{-2}
Air permeability†	90 Gurley s	3 Gurley s

* Average values, determined by cross-sectional SEM.
† Values provided by the manufacturer.

A CO_2 electrolyser with a zero-gap cathode half-cell configuration (see Fig. 1, details of the electrolyser were described previously in [7,38–41]) was used for the electrochemical reduction of CO_2. The Ag NW-coated GDEs were placed on the stainless steel body, with the Ag NW layer directed upwards. The such formed cathode was then covered by an anion exchange membrane (AEM, X37-50 RT, Dioxide materials), on top of which a PTFE chamber was placed to support the anolyte, a 2.0moldm^{--3} aqueous KOH solution (KOH, analytical grade, was purchased from Sigma Aldrich). A central orifice with a diameter of 3 mm at the bottom of the anode compartment provided contact between the anolyte and the membrane-cathode assembly, and the area of this opening (0.0707 cm^2) was considered the geometric surface area of the cathode, used for the normalization of current to current density. An iridium (Ir) wire (99.9%, MaTeck Material-Technologie & Kristalle GmbH, Germany) separated by a glass frit from the anolyte compartment, and a Ag|AgCl|3moldm^{--3} KCl electrode (double junction design, Metrohm) immersed directly into the anolyte were used as counter and reference electrodes. A humidified CO_2 stream (99.999%, Carbagas, Switzerland) was fed to the fibrous layer of the cathode from the backside of the cell at a constant volumetric flow rate of 18 cm^3 min^{-1}. Electrolyses were carried out using an ECi-200 potentiostat (Nordic Electrochemistry) at a constant current of −20 mA, resulting in a current density of −283 mA cm^{-2}, during which the formed gaseous reaction products were quantified by online gas chromatography (GC, SRI Instruments), as described elsewhere [7].

For the SEM and EDX studies presented in the paper, a Zeiss Gemini 450 SEM was applied, equipped with an InLens secondary electron (SE), a backscatter electron detector (BSD) and a SuperEDX detector.

Contact angle measurements were carried out using a Krüss Advance Drop Shape Analyzer DSA25 (Krüss GmbH, Hamburg, Germany). Electrodes were mounted on a flat stage and water drops (milli-Q water, 1.4 $\mu\ell$) were deposited at room temperature.

Raw data, as well as unprocessed measurement files serving as a basis of this publication can be downloaded from Zenodo [42].

4. Demonstrative experiments

Two gas diffusion electrodes —one supported by a Freudenberg H23C8 paper (GDL#1), and another by a Sigracet 36BB paper (GDL#2)— were created and used in our experiments. The two GDLs, as can be seen in Table 1, are of different structure, and the majority of differences arise from that while the microporous layer of GDL#1 is thinner but more compact (Fig. 4.a), the relatively thick microporous layer of GDL#2 is laced by small cracks that are visible also to the bare eye (Fig. 4.b).

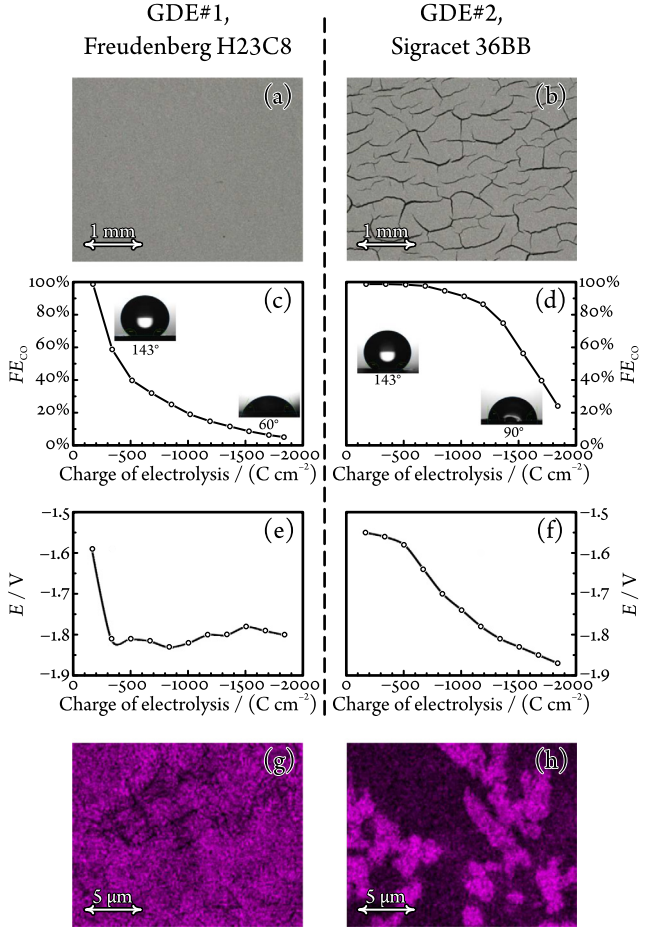

Fig. 4. The top-down optical microscopy image of the two studied gas diffusion electrodes exhibit a compact microporous layer in case of GDE#1 (a), while the top surface of GDE#2 (b) is laced by small cracks. Both GDEs exhibit severe stability losses (a decrease of the Faradaic efficiency of CO production as a function of the passed charge) when made subject to electrolysis at a constant current density of –283 mA cm^{-2}. While GDE#1 quickly loses stability (c), GDE#2 remains stable for longer time (d). The hydrophobicity of both GDLs decrease heavily during prolonged *ec*-CO_2RR stressing (consumed charge: –1839 C cm^{-2}), as revealed by the pre- and post-electrolysis contact angle measurements shown in the insets of (c) and (d). The shift from *ec*-CO_2RR to HER is also indicated by changes of the measured electrode potentials shown in panels (e) and (f). That the mentioned hydrophobicity loss is caused by the appearance of K_2CO_3 or $KHCO_3$ precipitates on-top of both GDEs during electrolysis is clearly shown by the top-down EDX elemental maps of (g) and (h), recorded after the total charge of –1839 C cm^{-2} is passed through the GDEs.

When made subject to constant-current electrolyses experiments (applied current density: –283 mA cm^{-2}), both GDEs initially produce CO at close to 100% Faradaic efficiency. As the electrolysis continues to longer times, the observed Faradaic efficiency however drops down (Fig. 4.c and 4.d), and the observed stability loss commences earlier in case of GDE#1 (with the compact structure) than in case of GDE#2 (having a cracked microporous layer).

The observed efficiency loss is due to the flooding of the GDEs, which can be inferred not only from pre- and post-electrolysis sessile drop goniometry that clearly demonstrates a significant decrease of the surface hydrophobicity during electrolysis (insets of Fig. 4.c and 4.d), but also from top-down EDX elemental mapping that exhibits the formation of massive amounts of K_2CO_3/$KHCO_3$ precipitates on top of both GDE samples (Fig. 4.e and 4.f).

These top-down EDX elemental maps provide a straightforward explanation of the observed stability differences: while at the end of electrolysis, GDE#1 is more or less uniformly covered by K_2CO_3/$KHCO_3$ precipitates (and it is safe to assume that this uniform precipitate layer practically blocks all active Ag catalyst sites), we observe a rather non-uniform coverage (and an only partially blocked catalytic activity) in case of GDE#2. As to why the two GDEs are covered differently by the formed carbonate precipitates, top-down EDX mapping provides no answer, however. In order to address this question we have to rely on the combined cross-sectional EDX/ICP–MS method described previously in Section 2.

When GDE samples are made subject to electrolyses consuming different amounts of charge, and the samples are processed as was shown before in Fig. 3, the obtained absolute concentration *vs.* depth profiles are those shown by Fig. 5. Based on these profiles, a very important observation can be made: namely, that the total amount of formed precipitates, as well as the extent to which they penetrate the GDE structure is markedly different on GDE#1 and #2.

On GDE#1 —with the compact surface— K_2CO_3 and $KHCO_3$ precipitates are mainly formed (and remain) inside the catalyst layer and inside the pores of the microporous layer, and appear only in little amount in the underlying (fibrous) structure. As the microporous layer has a very limited capacity to store the formed carbonates —note that with increasing charge, the concentration profiles seem to saturate—, catalytic sites become blocked, and this results in the quick break-down of the measured Faradaic efficiency (cf. to Fig. 4.c). This saturation effect can well be observed in case of GDE#1, where at charges of −510.0 C cm^{-2} and −1839 C cm^{-2} the K concentration distribution (Fig. 5) within the microporous layer varies only a little, while the Faradaic efficiency of CO production is already significantly lowered at −510.0 C cm^{-2}. In case of GDE#2, the (cracked) microporous layer has a higher capacity to store potassium precipitates, and saturation of the microporous layer (resulting in a significant decrease of the Faradaic efficiency) seems to occur only at −1839 C cm^{-2}.

The higher durability of GDE#2 is probably a result of the presence of cracks in its microporous layer. These cracks allow a direct access of electrolyte solution to the fibrous layer, hence carbonates will also be able to precipitate in deeper parts of the GDE structure. Neither the electrolyte that penetrates the fibrous layer, nor the carbonate crystals which are formed there will block the active catalytic sites on-top of the microporous layer. As a result, the break-down of the Faradaic efficiency of CO production will commence on GDE#2 much later than on GDE#1, since in the (due to the

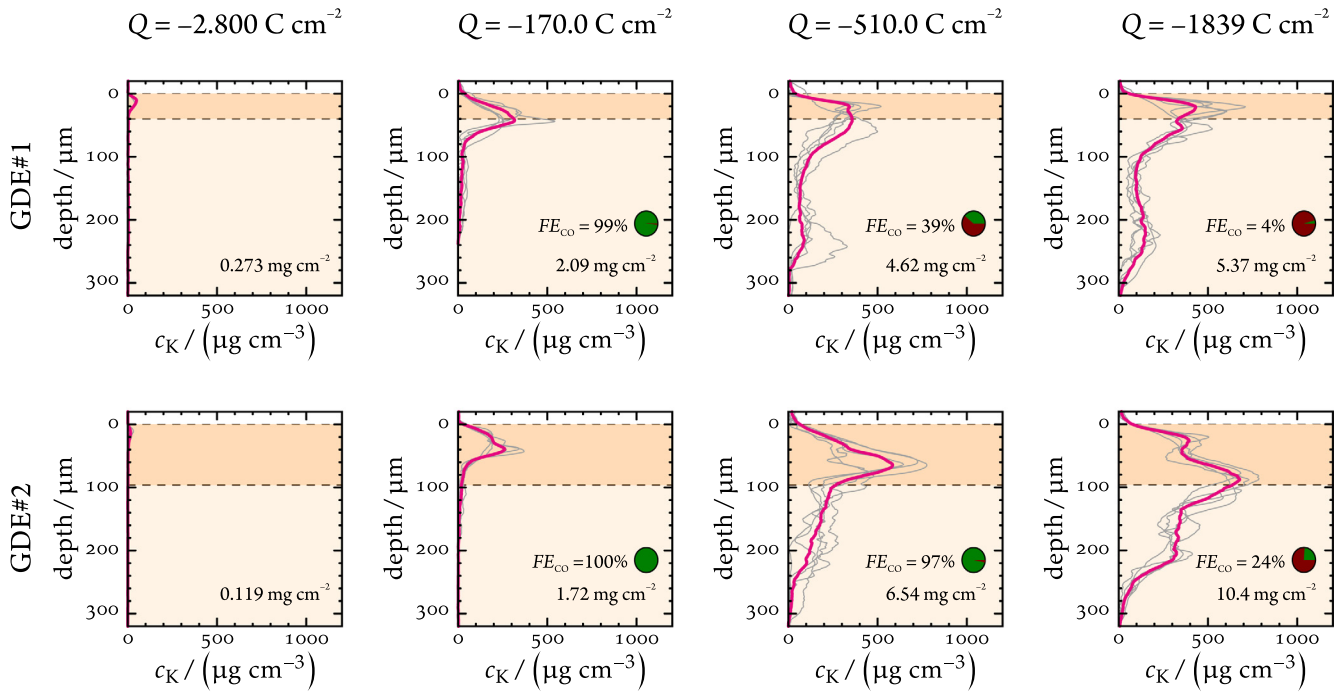

Fig. 5. Depth profiles of the absolute K^+ concentrations in different GDE samples, following electrolyses consuming different charges. The profiles were created by the cross-sectional EDX mapping/ICP–MS combination described in Section 2. (Grey curves show individual, magenta curves the averaged profiles.) The integral of each profile —that is, the total potassium content of the GDE normalised to surface area, determined by ICP–MS—, as well as the Faradaic efficiency of CO production, measured at the moment before the electrolysis was stopped, is given in each panel. The background shading of the panels pictures the GDL as a bi-layer structure (darker shading corresponds to the mic.roporous layer).

cracks, more penetrable) structure of GDE#2 a significantly bigger amount of K^+-containing precipitates has to be formed to effectively block the access of CO_2 to the catalyst layer. In case of GDE#1, blockage to the same effect occurs earlier, as in the absence of eluviation accelerating cracks, the formed precipitates quickly reach a critical concentration in the microporous layer.

Our results thus demonstrate that the crackedness of the GDL surface (maybe, somewhat counter-intuitively) plays a seemingly beneficial role in the water management of the GDE.

5. Conclusion

When *ec*-CO_2RR is carried out in a gas-fed CO_2 electrolyser with a zero-gap cathode half-cell configuration, K_2CO_3/$KHCO_3$ precipitation inside the GDE structure is a sovereign symptom (and probably an important driving force) of flooding. By determining, following electrolysis, the concentration distribution of carbonate salt leftovers within a GDE, we can assess the extent of flooding that occurred during the operation of the electrolyser, and we can better explain any observed stability losses and electrolyser malfunctions.

In this paper, a robust analytical method, based on the combination of cross-sectional EDX elemental mapping and ICP–MS-based analysis, was suggested in order to achieve the above goal. The novelty of this combination is that by ICP–MS measurements we turn EDX elemental —an essentially qualitative technique— into a quantitative characterisation tool that makes the obtained concentration profiles comparable across different GDE samples.

The basic concept and the technical details of the method were accurately described in the paper, and we also presented a short case study that demonstrated the applicability of the method.

We prepared two gas diffusion electrodes (one with a compact, another with a cracked microporous layer support) and made these subject to *ec*-CO_2RR stressing. We found that while the GDE with the compact surface looses stability (in terms of CO producing efficiency) rather quickly, the one with the cracked surface preserves its stability for a longer time. The newly developed, cross-sectional EDX elemental mapping/ICP–MS-based depth profiling tool provided an insight to the background of these efficiency losses. We found that the fibrous layer of GDEs (provided that it is accessible to water through the cracks of the microporous layer) may act as a reservoir for flooding, and as such, it can prevent (or at least postpone) the flooding-related deactivation of the catalyst layer.

The EDX/ICP–MS-based K precipitation mapping approach described in this paper will in future be used for the creation of statistically meaningful datasets based on which a systematic comparison of various gas diffusion layers and catalyst design concepts can be carried out.

Declaration of Competing Interest

The authors declare that they have no known competing financial interests or personal relationships that could have appeared to influence the work reported in this paper.

Acknowledgement

This publication was created as part of NCCR Catalysis (Grant No. 180544), a National Centre of Competence in Research funded by the Swiss National Science Foundation. V. Kolivoška acknowledges financial support from the Czech Science Foundation (project number 18-09848S). S. Vesztergom acknowledges support from the National Research, Development and Innovation Office of Hungary (NKFIH grant FK135375). Y. Kong, M. Liu and H. Hu acknowledge the financial support by the Chinese Scholarship Council (CSC).

References

[1] C. Hepburn, E. Adlen, J. Beddington, E.A. Carter, S. Fuss, N.M. Dowell, J.C. Minx, P. Smith, Ch.K. Williams, The technological and economic prospects for CO_2 utilization and removal, Nature 575 (7781) (2019) 87–97, https://doi.org/10.1038/s41586-019-1681-6.

[2] C.A.R. Pappijn, M. Ruitenbeek, M.-F. Reyniers, K.M. Van Geem, Challenges and opportunities of carbon capture and utilization: Electrochemical conversion of CO_2 to ethylene, Front. Energy Res. 8 (2020) 557466, https://doi.org/10.3389/fenrg.2020.557466.

[3] B. Endrődi, G. Bencsik, F. Darvas, R. Jones, K. Rajeshwar, Cs. Janáky, Continuous-flow electroreduction of carbon dioxide, Prog. Energy Combust. Sci. 62 (2017) 133–154, https://doi.org/10.1016/j.pecs.2017.05.005.

[4] J.-B. Vennekoetter, R. Sengpiel, M. Wessling, Beyond the catalyst: How electrode and reactor design determine the product spectrum during electrochemical CO_2 reduction, Chem. Engin. J. 364 (2019) 89–101, https://doi.org/10.1016/j.cej.2019.01.045.

[5] Y. Gu, J. Wei, X. Wu, X. Liu, A study on improving the current density performances of CO_2 electrolysers, Sci. Rep. 11 (2021) 11136, https://doi.org/10.1038/s41598-021-90581-0.

[6] B. Jung, S. Park, C. Lim, W.H. Lee, Y. Lim, J. Na, Ch.-J. Lee, H.-S. Oh, U. Lee, Design methodology for mass transfer-enhanced large-scale electrochemical reactor for CO_2 reduction, Chem. Eng. J. 424 (2021) 130265, https://doi.org/10.1016/j.cej.2021.130265.

[7] M.deJ. Gálvez-Vázquez, P. Moreno-García, H. Xu, Y. Hou, H. Hu, I.Z. Montiel, A. V. Rudnev, Sh. Alinejad, V. Grozovski, B.J. Wiley, M. Arenz, P. Broekmann, Environment matters: CO_2RR electrocatalyst performance testing in a gas-fed zero-gap electrolyzer, ACS Catal. 10 (2020) 13096–13108, https://doi.org/10.1021/acscatal.0c03609.

[8] K. Yang, R. Kas, W.A. Smith, Th. Burdyny, Role of the carbon-based gas diffusion layer on flooding in a gas diffusion electrode cell for electrochemical CO_2 reduction, ACS Energy Lett. 6 (2020) 33–40, https://doi.org/10.1021/acsenergylett.0c02184.

[9] M.E. Leonard, L.E. Clarke, A. Forner-Cuenca, S.M. Brown, F.R. Brushett, Investigating electrode flooding in a flowing electrolyte, gas-fed carbon dioxide electrolyzer, ChemSusChem 13 (2) (2019) 400–411, https://doi.org/10.1002/cssc.201902547.

[10] M.E. Leonard, M.J. Orella, N. Aiello, Y. Román-Leshkov, A. Forner-Cuenca, F.R. Brushett, Flooded by success: On the role of electrode wettability in CO_2 electrolyzers that generate liquid products, J. Electrochem. Soc. 167 (2020) 124521, https://doi.org/10.1149/1945-7111/abaa1a.

[11] B. Endrődi, A. Samu, E. Kecsenovity, T. Halmágyi, D. Sebők, Cs. Janáky, Operando cathode activation with alkali metal cations for high current density operation of water-fed zero-gap carbon dioxide electrolysers, Nature Energy 6 (2021) 439–448, https://doi.org/10.1038/s41560-021-00813-w.

[12] Z. Xing, X. Hu, X. Feng, Tuning the microenvironment in gas-diffusion electrodes enables high-rate CO_2 electrolysis to formate, ACS Energy Lett. 6 (2021) 1694–1702, https://doi.org/10.1021/acsenergylett.1c00612.

[13] Z. Xing, L. Hu, D.S. Ripatti, X. Hu, X. Feng, Enhancing carbon dioxide gas-diffusion electrolysis by creating a hydrophobic catalyst microenvironment, Nature Comm. 12 (2021) 1–11, https://doi.org/10.1038/s41467-020-20397-5.

[14] B. Kim, F. Hillman, M. Ariyoshi, S. Fujikawa, P.J.A. Kenis, Effects of composition of the micro porous layer and the substrate on performance in the electrochemical reduction of CO_2 to CO, J. Power Sources 312 (2016) 192–198, https://doi.org/10.1016/j.jpowsour.2016.02.043.

[15] W.H. Lee, Y.-J. Ko, Y. Choi, S.Y. Lee, C.H. Choi, Y.J. Hwang, B.K. Min, P. Strasser, H.-S. Oh, Highly selective and scalable CO_2 to CO - electrolysis using coral-nanostructured Ag catalysts in zero-gap configuration, Nano Energy 76 (2020) 105030, https://doi.org/10.1016/j.nanoen.2020.105030.

[16] U.O. Nwabara, A.D. Hernandez, D.A. Henckel, X. Chen, E.R. Cofell, M.P. de Heer, S. Verma, A.A. Gewirth, P.J.A. Kenis, Binder-focused approaches to improve the stability of cathodes for CO_2 electroreduction, ACS Appl. Energy Mater. 4 (2021) 5175–5186, https://doi.org/10.1021/acsaem.1c00715.

[17] A. Reyes, R.P. Jansonius, B.A.W. Mowbray, Y. Cao, D.G. Wheeler, J. Chau, D.J. Dvorak, C.P. Berlinguette, Managing hydration at the cathode enables efficient CO_2 electrolysis at commercially relevant current densities, ACS Energy Lett. 5 (2020) 1612–1618, https://doi.org/10.1021/acsenergylett.0c00637.

[18] F. Bienen, J. Hildebrand, D. Kopljar, N. Wagner, E. Klemm, K.A. Friedrich, Importance of time-dependent wetting behavior of gas-diffusion electrodes for reactivity determination, Chem. Ing. Tech. 93 (2021) 1015–1019, https://doi.org/10.1002/cite.202000192.

[19] B. De Mot, J. Hereijgers, M. Duarte, T. Breugelmans, Influence of flow and pressure distribution inside a gas diffusion electrode on the performance of a flow-by CO_2 electrolyzer, Chem. Eng. J. 378 (2019) 122224, https://doi.org/10.1016/j.cej.2019.122224.

[20] B. Endrődi, E. Kecsenovity, A. Samu, F. Darvas, R.V. Jones, V. Török, A. Danyi, Cs. Janáky, Multilayer electrolyzer stack converts carbon dioxide to gas products at high pressure with high efficiency, ACS Energy Lett. 4 (2019) 1770–1777, https://doi.org/10.1021/acsenergylett.9b01142.

[21] D.G. Wheeler, B.A.W. Mowbray, A. Reyes, F. Habibzadeh, J. He, C.P. Berlinguette, Quantification of water transport in a CO_2 electrolyzer, Energy Environ. Sci. 13 (12) (2020) 5126–5134, https://doi.org/10.1039/d0ee02219e.

[22] D. McLaughlin, M. Bierling, R. Moroni, Ch. Vogl, G. Schmid, S. Thiele, Tomographic reconstruction and analysis of a silver CO_2 reduction cathode, Adv. Energy Mater. 10 (19) (2020) 2000488, https://doi.org/10.1002/aenm.202000488.

[23] F. Bienen, D. Kopljar, A. Löwe, S. Geiger, N. Wagner, E. Klemm, K.A. Friedrich, Revealing mechanistic processes in gas-diffusion electrodes during CO_2 reduction via impedance spectroscopy, ACS Sustainable Chem. Eng. 8 (2020) 13759–13768, https://doi.org/10.1021/acssuschemeng.0c04451.

[24] E.R. Cofell, U.O. Nwabara, S.S. Bhargava, D.E. Henckel, P.J.A. Kenis, Investigation of electrolyte-dependent carbonate formation on gas diffusion electrodes for CO_2 electrolysis, ACS Appl. Mater. Interfaces 13 (2021) 15132–15142, https://doi.org/10.1021/acsami.0c21997.

[25] B. De Mot, M. Ramdin, J. Hereijgers, Th.J.H. Vlugt, T. Breugelmans, Direct water injection in catholyte-free zero-gap carbon dioxide electrolyzers, ChemElectroChem 7 (2020) 3839–3843, https://doi.org/10.1002/celc.202000961.

[26] D. Raciti, T. Braun, B.M. Tackett, H. Xu, M. Cruz, B.J. Wiley, Th.P. Moffat, High-aspect-ratio Ag nanowire mat electrodes for electrochemical CO production from CO_2, ACS Catal. 11 (2021) 11945–11959, https://doi.org/10.1021/acscatal.1c02783.

[27] A.J. Welch, A.Q. Fenwick, A. Böhme, H.-Y. Chen, I. Sullivan, X. Li, J.S. DuChene, C. Xiang, H.A. Atwater, Operando local pH measurement within gas diffusion electrodes performing electrochemical carbon dioxide reduction, J. Phys. Chem. C 125 (2021) 20896–20904, https://doi.org/10.1021/acs.jpcc.1c06265.

[28] H.-R. Jhong, F.R. Brushett, P.J.A. Kenis, The effects of catalyst layer deposition methodology on electrode performance, Adv. Energy Mater. 3 (2013) 589–599, https://doi.org/10.1002/aenm.201200759.

[29] H. Haspel, J. Gascon, Is hydroxide just hydroxide? Unidentical CO_2 hydration conditions during hydrogen evolution and carbon dioxide reduction in zero-gap gas diffusion electrode reactors, ACS Appl. Energy Mater. 4 (2021) 8506–8516, https://doi.org/10.1021/acsaem.1c01693.

[30] S. Verma, B. Kim, H.-R. Jhong, S. Ma, P.J.A. Kenis, A gross-margin model for defining technoeconomic benchmarks in the electroreduction of CO_2, ChemSusChem 9 (2016) 1972–1979, https://doi.org/10.1002/cssc.201600394.

[31] N.T. Nesbitt, Th. Burdyny, H. Simonson, D. Salvatore, D. Bohra, R. Kas, W.A. Smith, Liquid–solid boundaries dominate activity of CO_2 reduction on gas-diffusion electrodes, ACS Catal. 10 (2020) 14093–14106, https://doi.org/10.1021/acscatal.0c03319.

[32] T. Luo, S. Abdu, M. Wessling, Selectivity of ion exchange membranes: A review, J. Membr. Sci. 555 (2018) 429–454, https://doi.org/10.1016/j.memsci.2018.03.051.

[33] R. Wang, H. Haspel, A. Pustovarenko, A. Dikhtiarenko, A. Russkikh, G. Shterk, D. Osadchii, S. Ould-Chikh, M. Ma, W.A. Smith, K. Takanabe, F. Kapteijn, J. Gascon, Maximizing Ag utilization in high-rate CO_2 electrochemical reduction with a coordination polymer-mediated gas diffusion electrode, ACS Energy Lett. 4 (2019) 2024–2031, https://doi.org/10.1021/acsenergylett.9b01509.

[34] M. Liu, Y. Kong, H. Hu, N. Kovács, Ch. Sun, I.Z. Montiel, M.deJ. Gálvez Vázquez, Y. Hou, M. Mirolo, I. Martens, J. Drnec, S. Vesztergom, P. Broekmann, The capping agent is the key: Structural alterations of Ag NPs during CO_2 electrolysis probed in a zero-gap gas-flow configuration, J. Catal. 404 (2021) 371–382, https://doi.org/10.1016/j.jcat.2021.10.016.

[35] J.J. Friel, Ch.E. Lyman, Tutorial review: X-ray mapping in electron-beam instruments, Microsc. Microanal. 12 (2006) 2–25, https://doi.org/10.1017/s1431927606060211.

[36] N.J. Firet, Th. Burdyny, N.T. Nesbitt, S. Chandrashekar, A. Longo, W.A. Smith, Copper and silver gas diffusion electrodes performing CO_2 reduction studied through operando X-ray absorption spectroscopy, Catal. Sci. Technol. 10 (2020) 5870–5885, https://doi.org/10.1039/d0cy01267j.

[37] H. Hu, M. Liu, Y. Kong, N. Mysuru, Ch. Sun, M.deJ. Gálvez-Vázquez, U. Müller, R. Erni, V. Grozovski, Y. Hou, P. Broekmann, Activation matters: Hysteresis effects during electrochemical looping of colloidal ag nanowire catalysts, ACS Catal. 10 (2020) 8503–8514, https://doi.org/10.1021/acscatal.0c02026.

[38] M.deJ. Gálvez Vázquez, Sh. Alinejad, H. Hu, Y. Hou, P. Moreno-García, A. Zana, G.K.H. Wiberg, P. Broekmann, M. Arenz, Testing a silver nanowire catalyst for the selective CO_2 reduction in a gas diffusion electrode half-cell setup enabling high mass transport conditions, Chimia 73 (2019) 922–927, https://doi.org/10.2533/chimia.2019.922.

[39] Sh. Alinejad, J. Quinson, G.K.H. Wiberg, N. Schlegel, D. Zhang, Y. Li, S. Reichenberger, St. Barcikowski, M. Arenz, Electrochemical reduction of CO_2 on Au electrocatalysts in a zero-gap, half-cell gas diffusion electrode setup: a systematic performance evaluation and comparison to a H-cell setup, in: ChemRxiv, Cambridge Open Engage, 2021. https://doi.org/10.33774/chemrxiv-2021-1t50s-v3.

[40] G.K.H. Wiberg, M. Fleige, M. Arenz, Gas diffusion electrode setup for catalyst testing in concentrated phosphoric acid at elevated temperatures, Rev. Sci. Instrum. 86 (2015) 024102, https://doi.org/10.1063/1.4908169.

[41] M. Inaba, A.W. Jensen, G.W. Sievers, M. Escudero-Escribano, A. Zana, M. Arenz, Benchmarking high surface area electrocatalysts in a gas diffusion electrode: Measurement of oxygen reduction activities under realistic conditions, Energy Environ. Sci. 11 (2018) 988–994, https://doi.org/10.1039/c8ee00019k.

[42] Y. Kong, H. Hu, M. Liu, Y. Hou, V. Kolivoška, S. Vesztergom, P. Broekmann, Raw data for the article Visualisation and quantification of flooding phenomena in gas diffusion electrodes used for electrochemical CO_2 reduction: A combined EDX/ICP–MS approach (2022). https://doi.org/10.5281/ZENODO.6037503.